

# Sol–Gel Transitions and Liquid Crystal Phase Transitions in Concentrated Aqueous Suspensions of Colloidal Gibbsite Platelets

Maurice C. D. Mourad,<sup>\*,†</sup> Dmytro V. Byelov,<sup>†</sup> Andrei V. Petukhov,<sup>†</sup> D. A. Matthijs de Winter,<sup>‡</sup> Arie J. Verkleij,<sup>‡</sup> and Henk N. W. Lekkerkerker<sup>†</sup>

van 't Hoff Laboratory for Physical and Colloid Chemistry, Faculty of Sciences, Utrecht University, P.O. Box 80.056, 3508 TB Utrecht, The Netherlands, and Electron Microscopy and Structure Analysis, Cellular Architecture and Dynamics, Faculty of Sciences, Utrecht University, P.O. Box 80.051, 3508 TB Utrecht, The Netherlands

Received: April 24, 2009; Revised Manuscript Received: July 8, 2009

In this paper, we present a comprehensive study of the sol–gel transitions and liquid crystal phase transitions in aqueous suspensions of positively charged colloidal gibbsite platelets at pH 4–5 over a wide range of particle concentrations (50–600 g/L) and salt concentrations ( $10^{-4}$ – $10^{-1}$  M NaCl). A detailed sol–gel diagram was established by oscillatory rheological experiments. These demonstrate the presence of kinetically arrested states both at high and at low salt concentrations, enclosing a sol region. Birefringence and iridescence show that in the sol state nematic and hexagonal columnar liquid crystal phases are formed. The gel and liquid crystal structures are studied in further detail using small-angle X-ray scattering (SAXS) and cryo-focused ion beam/scanning electron microscopy (cryo-FIB-SEM). The gel formed at high salt concentration shows signatures of a sponge-like structure and does not display birefringence. In the sol region, by lowering the salt concentration and/or increasing the gibbsite concentration, the nematic phase gradually transforms from the discotic nematic ( $N_D$ ) into the columnar nematic ( $N_C$ ) with much stronger side-to-side interparticle correlations. Subsequently, this  $N_C$  structure can be either transformed into the hexagonal columnar phase or arrested into a birefringent repulsive gel state with  $N_C$  structure.

## 1. Introduction

Sol–gel transitions and liquid crystal phase transitions in aqueous suspensions of charged colloidal platelets, ranging from natural<sup>1–6</sup> and synthetic clays<sup>1,7–12</sup> to hydroxides (nickel hydroxide<sup>13</sup> and aluminum hydroxide<sup>14,15</sup>) and layered double hydroxides (takovite<sup>16</sup> and hydrotalcite<sup>17</sup>), have attracted significant attention during the last 15 years.

A particularly well studied class of charged colloidal particles is that of clay platelets. The propensity of suspensions of clay platelets to form gels is well-known, widely studied, and exploited extensively in industry.<sup>18</sup> While rheological measurements in the early 1950s indicated a minimum in the yield stress as a function of salt concentration in clay sols,<sup>19</sup> it has only been in the last 10 years clearly recognized that clays are in a gel state both at high and at low concentrations of salt, while at intermediate salt concentrations for the same clay content a sol state is found.<sup>2</sup>

This sequence of repulsive gel–sol–attractive gel states upon an increase of the salt concentration has also been reported for aqueous suspensions of gibbsite<sup>20</sup> and hydrotalcite platelets.<sup>17</sup> An account of this gelation behavior has been put forward in terms of the domination of either attractive or repulsive interactions.<sup>21–23</sup> At low salt, the interaction is strongly repulsive and the dispersion appears as a repulsive gel. With increasing salt concentration, the repulsion is weakened and the dispersion appears as a sol. A further increase of the salt concentration

leads to a second gel state (attractive gel) governed by attractive interactions between the platelets. Another characteristic feature of suspensions of anisometric colloidal particles is their ability to form liquid crystals. In the 1940s, Onsager<sup>24</sup> showed that for such systems entropy is responsible for the phase separation into an isotropic (I) and nematic (N) phase. The balance between orientational entropy (favoring the isotropic phase) and excluded volume entropy (favoring the nematic phase) gives rise to a stable nematic phase at higher particle concentrations. Until very recently, reports on the isotropic–nematic (I–N) transition in systems of plate-like particles were particularly rare in the literature. In fact, the I–N transition in clay platelets—which was reported initially by Langmuir<sup>25</sup> and inspired Onsager to extend his theory to platelets—is generally obscured by the interference of gelation. Starting in the 1990s, emphasis was placed on Laponite,<sup>26</sup> a synthetic Hectorite, in an attempt to circumvent the poorly understood behavior of natural clays. However, the main result from persevering investigations on the phase behavior of these suspensions is that gelation is again ubiquitous.<sup>1,7,9,12</sup> Meanwhile, it turned out that more valuable model systems for charged platelets, displaying both liquid crystal transitions and sol–gel transitions, are Na fluorohectorite,<sup>11</sup> gibbsite,<sup>14,15</sup> and mixed-metal hydroxides.<sup>17</sup> A breakthrough came with the recent work of Michot et al., who observed I–N phase separation and the sol–gel transition in suspensions of the *natural* clays nontronite<sup>4,6</sup> and beidellite,<sup>27</sup> dioctahedral smectite clays with ionic substitutions in the tetrahedral layer.

However, the relation between the I–N transition (or more generally, liquid crystal phase transitions) and the sol–gel transition remains an unresolved issue. To address this issue, we present a multitechnique study of the sol–gel and liquid

\* To whom correspondence should be addressed. E-mail: m.c.d.mourad@uu.nl.

<sup>†</sup> van 't Hoff Laboratory for Physical and Colloid Chemistry.

<sup>‡</sup> Electron Microscopy and Structure Analysis, Cellular Architecture and Dynamics.

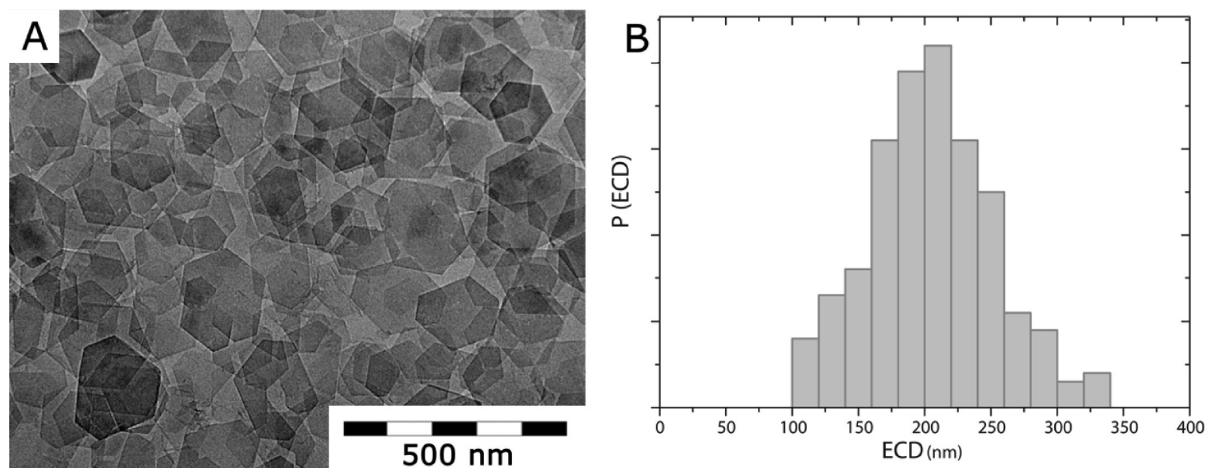


**Figure 1.** (A) Transmission electron micrograph of colloidal gibbsite platelets. (B) Histogram of the equivalent circular diameter (ECD) of the platelet surface as determined from transmission micrographs.

crystal phase transitions of aqueous suspensions of colloidal gibbsite platelets, over a wide range of particle concentrations and salt concentrations. To elucidate the nature of the liquid crystal and kinetically arrested states of gibbsite platelets, we have used polarized light techniques, oscillatory rheological measurements, small angle X-ray scattering (SAXS) measurements, and focused ion beam/scanning electron microscopy under cryogenic conditions (cryo-FIB-SEM). From SAXS and cryo-FIB-SEM measurements, we obtain a structure of the attractive gel that has great similarity to that in clay systems, although for gibbsite it is observed at a higher salt concentration. In the sol region, we observe isotropic-to-nematic (I–N) and nematic-to-columnar (N–C) liquid crystal transitions. From SAXS measurements, it follows that nematic phases of both the discotic nematic ( $N_D$ ) and the columnar nematic ( $N_C$ ) type occur. While in the sol region equilibria between  $N_C$  and C occur, the repulsive gel at large particle concentrations has the signature of a  $N_C$  phase. Apparently, the transition to the columnar phase is preempted by a transition to a repulsive gel state with a kinetically arrested, glassy nature and the structural features of the  $N_C$  phase.

## 2. Experimental Section

Colloidal gibbsite platelets were grown in acidic aqueous solution.<sup>28</sup> First, hydrochloric acid (0.09 M HCl, 37%, Merck), aluminum *sec*-butoxide (0.08 M, 95%, Fluka Chemika), and aluminum isopropoxide (0.08 M, 98+%, Acros Organics) were dissolved in demineralized water (15 L, equally divided over three Erlenmeyer flasks). The mixtures were mechanically stirred for 10 days and then heated in borosilicate reaction vessels that were immersed in a thermostatted water bath (85 °C for 72 h). Next, the colloidal dispersions were centrifuged (1200g, 15–20 h). The smallest gibbsite particles were then removed from the batch with the supernatant. The size of the gibbsite particles was analyzed by transmission electron microscopy (TEM). The two systems with smaller gibbsite particles were redispersed in aqueous solution (1.5 L) of hydrochloric acid, aluminum *sec*-butoxide, and aluminum isopropoxide (concentrations equal to those described above) and heated at 85 °C for 72 h in order to perform a seeded growth of the particles. The mixture was cooled down to room temperature and centrifuged again (1200g, 15–20 h). Finally the dispersions were added together and dialyzed against demineralized water in tubes of regenerated cellulose (Visking, MWCO 12 000–14 000) until the conductivity dropped to 20  $\mu$ S/cm. Finally, aluminum chlorohydrate

(0.6 g/g of gibbsite particles, Locron P, Hoechst AG, Germany) was added to the suspension to hydrolyze and form  $Al_{13}$  Keggin ions ( $[Al_{13}O_4(OH)_{24}(H_2O)_{12}]^{7+}$ ) and thereby increase the stability of the gibbsite platelets in water.<sup>29</sup>

**2.1. Particle Characterization.** The resulting suspension was analyzed for solid content and inspected with TEM (Figure 1). From the micrographs, the surface area of over 200 individual hexagonal particles was measured. An average equivalent circular diameter (ECD) was calculated as

$$ECD = \sqrt{\frac{4A}{\pi}} \quad (1)$$

where  $A$  is the measured surface area. Furthermore, the particle size distribution (Figure 1B) and the standard deviation ( $\sigma_{ECD}$ ) were determined. The yield of the entire synthesis was determined to be 58 g (dry particle weight) with  $ECD = 205$  nm ( $\sigma_{ECD} = 47$  nm).

**2.2. Sample Preparation and Optical Observations.** Concentrated gibbsite dispersions were prepared and set at ionic strength by centrifugation and redispersion in water with NaCl. Samples for visual observation were put in large capillaries (1.0  $\times$  10.0 mm cross section, Vitrotubes, VitroCom Inc.) that were flame-sealed. Visual inspection was performed on a regular basis. For this, a home-built polarization setup was used, consisting of two crossed polarizing filters that could be illuminated by a 150 W lamp in combination with a condenser lens and a ground glass diffuser for homogeneous illumination. For X-ray experiments, samples were transferred into round Mark tubes (Quartz, 2 mm diameter and about 10  $\mu$ m wall thickness, W. Müller, Berlin, Germany).

**2.3. Rheological Measurements.** Oscillatory experiments in the frequency range 0.01–100 Hz were performed on gibbsite suspensions using a Physica Anton Paar (MCR-300) controlled stress rheometer operating at a strain amplitude of 0.01. It was verified that at this strain amplitude the system was in the linear viscoelastic regime at all frequencies. A cone–plate measuring geometry was used having a diameter of 50 mm and a cone angle of 1°. The plate was kept at 20 °C by a connection with a thermostatic water bath. All measurements were initiated by a preshear (100 s at a shear rate of 500  $s^{-1}$ ). From the measurements, the frequency dependent storage ( $G'$ ) and loss modulus ( $G''$ ) components of complex shear modulus  $G^* = G' + iG''$  were determined.<sup>30</sup>

**2.4. Small-Angle X-ray Scattering.** X-ray studies were performed at the Dutch-Belgian beamline BM-26 DUBBLE of the European synchrotron radiation facility (ESRF) in Grenoble, France, 1 month after preparation. We used a microradian X-ray diffraction setup, similar to the one described in literature.<sup>31</sup> The X-ray beam was focused by a set of compound refractive lenses<sup>32</sup> (CRLs) at a phosphor screen of the CCD (charge-coupled device) X-ray detector (Photonic Science, 4008 × 2671 pixels of 22 μm square). Any focusing of the beam before the experimental hutch was avoided to achieve maximum transverse coherence length of the beam. The capillaries were placed just after the CRLs at a distance of about 8 m from the detector. This setup allows achieving an angular resolution of the order of 5–7 microradians. The X-ray photon energies of 13 keV (wavelength = 0.095 nm) were used. The beam diameter in the sample was about 0.5 mm.

**2.5. Cryo-Focused Ion Beam/Scanning Electron Microscopy.** Droplets of aqueous gibbsite suspensions were put in between two small copper rivets (dimensions 4.5 × 3 mm, BAL-TEC AG, Liechtenstein). The suspensions were then cryo-immobilized by plunge-freezing the copper hats in N<sub>2</sub> slush. Samples are transferred under vacuum to the cryostatic preparation chamber (Quorum Technologies, PP2000T, United Kingdom) that is attached to the focused ion beam/scanning electron microscope (FIB-SEM), where one of the copper parts is mechanically removed in order to expose the surface of the frozen suspension. The sample was then passed through on the cryostatic microscope chamber of the cryo-FIB-SEM (Nova Nanolab 600, FEI, The Netherlands) that was operated at 30 kV for the ions and 3 kV for the electrons. Here, the sample can be inspected with both focused ion beam and electron beam imaging. *In situ* sectioning of the sample was performed by milling with the focused ion beam, which is able to precisely cut through the frozen dispersion and its constituents and thereby create a cross section that is imaged by (high resolution) SEM.<sup>33</sup> It is important to inspect the structure of the suspension within the droplet rather than on the outer surface, as platelets (or in general, anisometric particles) behave and order differently on interfaces, which may therefore not be regarded as representative for the structure. In order to achieve this, cross sections that went micrometers deep into the specimen were obtained by ion milling in a two-step process. First, rough sectioning was performed by high current milling (5.0 nA). This step was followed by a low current polishing step (0.3 nA), which results in cross sections with a smooth surface. The structure of the gibbsite platelets as observed in cryo-FIB-SEM is compared with SAXS results, to exclude effects of the freezing and sectioning procedure on the samples from which micrographs were made.

### 3. Results

**3.1. Rheological Measurements.** The frequency dependences of the dynamic moduli  $G'$  and  $G''$  for aqueous gibbsite dispersions at ionic strengths of 10<sup>-1</sup>, 3 × 10<sup>-2</sup>, 10<sup>-2</sup>, 10<sup>-3</sup>, and 10<sup>-4</sup> M NaCl and gibbsite particle concentrations ranging from 50 to 600 g/L are presented in Figure 2. At salt concentrations of 10<sup>-1</sup> and 3 × 10<sup>-2</sup> M NaCl, the dynamic moduli are almost independent of frequency for all solid contents measured. For the lower salt concentrations,  $G'$  and  $G''$  depend on frequency for the lower particle concentrations (100 and 200 g/L). These suspensions are only moderately viscous, and there are no large differences between the values for  $G'$  and  $G''$ . At higher particle concentrations, the dynamic moduli are independent of frequency and eventually  $G'$  exceeds  $G''$ , sometimes even by an order of magnitude.

In case the value of  $G'$  exceeds  $G''$  and  $G'$  is of the order of 1 Pa or larger, this is a typical signature for the behavior of gels.<sup>3,34,35</sup> With the help of these criteria, sols and gels can be distinguished and the rheological state diagram can be constructed. This rheological state diagram is presented in Figure 3. We note that the shape of the rheological state diagram has the same shape as the rheological state diagrams experimentally determined for dispersions of natural clay,<sup>2,3,5</sup> synthetic clay,<sup>9</sup> and MgAl layered double hydroxides,<sup>17</sup> all of which are charged, plate-like particles. Hence, it appears that this kind of rheological state diagram is generic for dispersions of charged platelets.

**3.2. Optical Observations.** All samples with salt concentrations of 3 × 10<sup>-2</sup> M NaCl or smaller that were classified by the rheological criteria above as sols showed the first signs of the formation of birefringent phases within 1 day after preparation. The same behavior was observed for two samples at the border between the sol and the gel region (3 × 10<sup>-2</sup> M, 450 g/L, and 10<sup>-3</sup> M, 350 g/L) that were rheologically classified as gels. The other samples with salt concentrations of 3 × 10<sup>-2</sup> M NaCl or smaller that were classified as gels, while birefringent, show a somewhat different texture and no signs of phase separation. The gel character of these samples is demonstrated by the trapping of air bubbles in the dispersions. The samples with a salt concentration of 10<sup>-1</sup> M NaCl show different behavior. They remain isotropic and particularly at the lowest particle concentration expulsion of pure solvent from the gel (syneresis) started within 1 day after preparation.

All samples were inspected on a regular basis for a period of 2 years in order to observe changes in the suspensions. To exhibit the course of events, photographs of the flat sample cells between crossed polarizers, taken 1 month and 15 months after mixing, are presented in Figure 4. The observations presented in Figure 4 provide the location of the phase equilibria as a function of the overall gibbsite concentration and the salt concentration. After 1 month in the phase separating samples, a progression of liquid crystal phases ranging from I+N via N to N+C appeared. Due to the action of gravity, the volume of the individual phases and even the appearance of the hexagonal columnar phase as such depends on time, as is evidenced by the right-hand panels in Figure 4. Indeed, after 15 months, we observed liquid crystal phases ranging from I+N via I+N+C to N+C, reflecting the influence of gravity leading to sedimentation equilibria displaying multiple phases. Moreover, below the interfaces, the birefringent phases of phase separated samples lost turbidity and became more homogeneous. We did not measure the gibbsite concentrations in the individual phases which are, again due to gravity, height dependent. The outward appearance of the non-phase-separating samples with salt concentrations of 3 × 10<sup>-2</sup> M NaCl or smaller that were classified as gels did not seem to change.

In the samples with a salt concentration of 10<sup>-1</sup> M NaCl, syneresis continued for the samples at 50, 100, and 200 g/L, while the sample at 300 g/L apparently had a gel strength so high that no visible syneresis occurred.

**3.3. Small-Angle X-ray Scattering and Cryo Scanning Electron Microscopy.** The dispersions were examined by SAXS in order to obtain more information on the structure. These measurements were performed on 1 month old samples. While all samples contained in Figure 4 were measured by SAXS, here, we highlight the results of three representative series of samples. In the first series of samples, the scattering patterns from the sol region are discussed for a fixed gibbsite concentration of 300 g/L and salt concentrations that vary from 3 × 10<sup>-2</sup> M down to 10<sup>-4</sup> M. This series covers the isotropic, nematic,



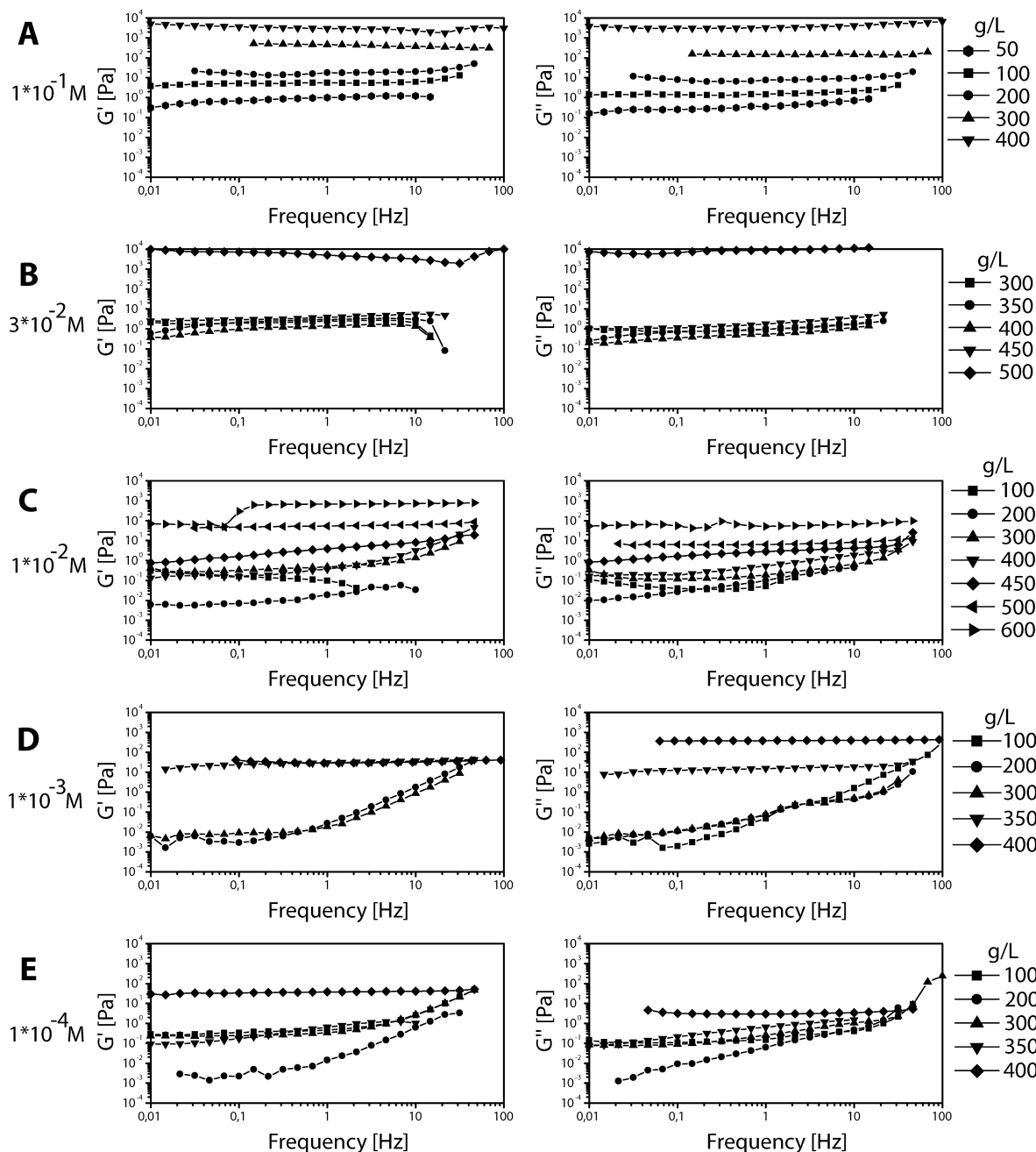


**Figure 2.** Rheological measurements on aqueous gibbsite suspensions. Evolution of  $G'$  (left panels) and  $G''$  (right panels) with the oscillatory frequency for particle concentration series at a salt concentration of (A)  $10^{-1}$  M, (B)  $3 \times 10^{-2}$  M, (C)  $10^{-2}$  M, (D)  $10^{-3}$  M, and (E)  $10^{-4}$  M.

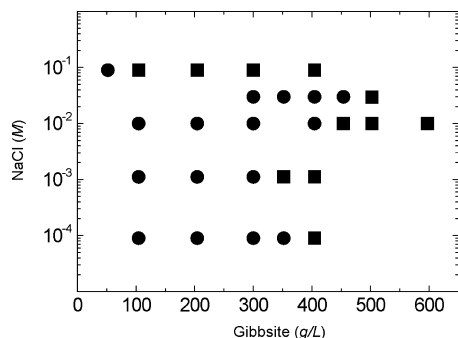


**Figure 3.** Sol-gel diagram of aqueous gibbsite dispersions, based on rheological measurements: (●) sol states; (■) gel states.

and hexagonal columnar liquid crystal phases (see Figure 4). Second, the influence of an increase of the gibbsite concentration

on the phase behavior is demonstrated by a series at a fixed salt concentration of  $10^{-2}$  M. Finally, in order to illustrate the structure of the system in the gel phase at high salt concentration ( $10^{-1}$  M), we present the results obtained for the samples with particle concentrations of 100 and 200 g/L.

The scattering patterns of the first series of samples at the fixed gibbsite concentration of 300 g/L are shown in Figure 5. Profiles obtained by azimuthal integration of these patterns are displayed in Figure 6. The sample at a salt concentration of  $3 \times 10^{-2}$  M displays phase separation in an isotropic (top) and a nematic (bottom) phase. Figure 5A displays the scattering pattern from the isotropic phase. We cannot detect any sign of anisotropy, and the scattering intensity decays monotonically.

For the nematic phase, lower in the capillary, the scattering pattern possesses anisotropy (see Figure 5B). This effect originates from the orientational ordering of the gibbsite

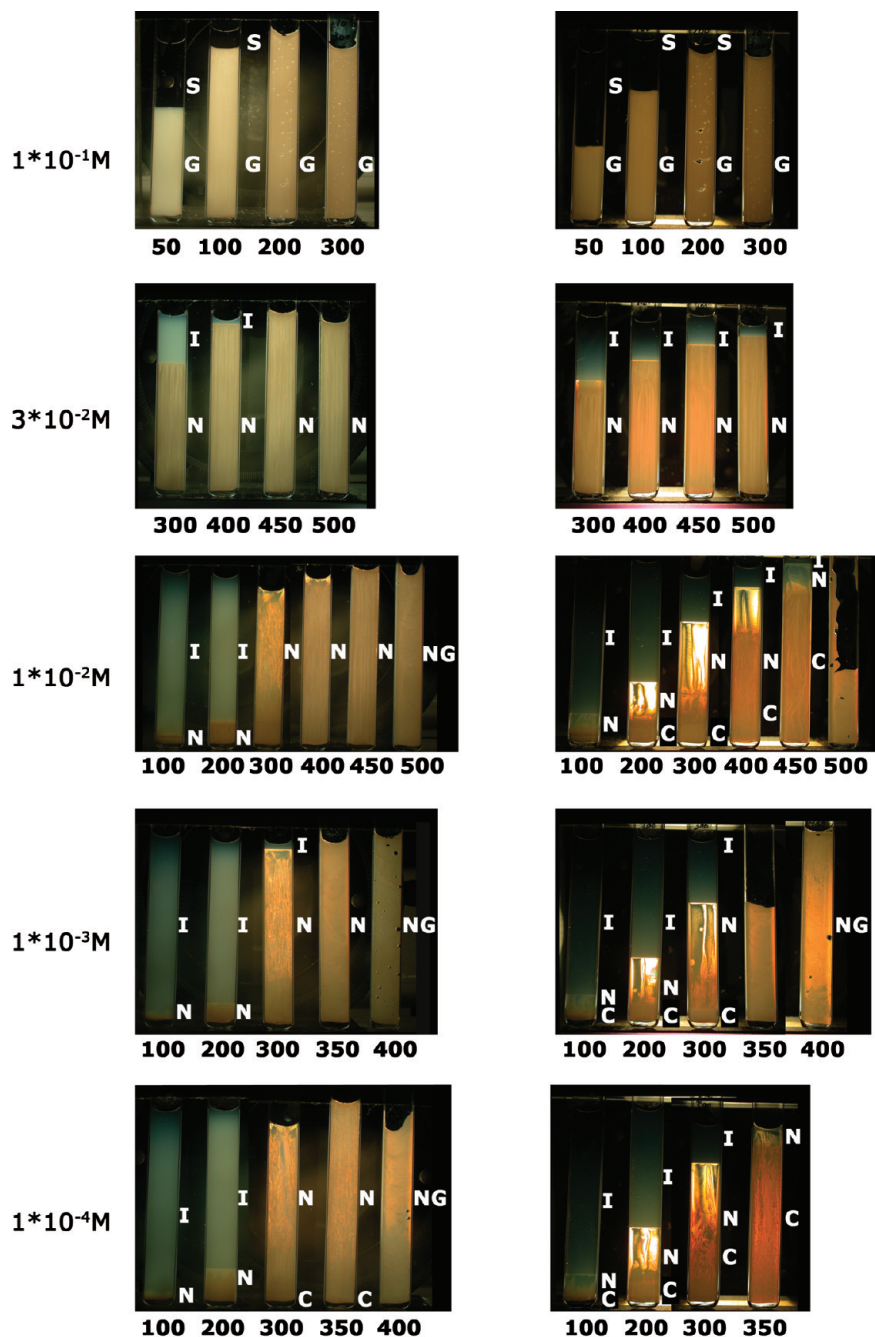


**Figure 4.** Aqueous gibbsite suspensions observed in crossed polarizers with back illumination. The panels on the left-hand side display the gibbsite concentration series at decreasing salt strengths, 1 month after preparation, while the panels on the right-hand side display the same series 15 months after preparation. At the left-hand side, the salt concentrations are indicated, while particle concentrations are displayed below each sample (in g/L). Phases are labeled S for solvent, G for (attractive) gel, I for isotropic, N for nematic, C for hexagonal columnar, and NG for nematic, repulsive gel.

platelets. The scattering intensity does not display any maximum, which indicates the absence of any pronounced positional correlations between the platelets. The pattern can be identified as discotic nematic ( $N_D$ ).<sup>36</sup> For the sample with an ionic strength of  $10^{-2}$  M, the scattering pattern is given in Figure 5C. The pattern possesses clear anisotropy, and a pronounced broad peak is observed at  $q = 0.118 \text{ nm}^{-1}$ . This implies the presence of  $N_D$  structure in the sample with face-to-face correlation distances between the platelets of 53 nm. An even richer scattering pattern can be seen in the sample upon decreasing the ionic strength to  $10^{-3}$  M. In Figure 5D, one can again see clear anisotropy in the pattern and a pronounced broad peak at  $q = 0.125 \text{ nm}^{-1}$ , which indicates a face-to-face distance between the platelets of

50 nm. Moreover, one can now observe an additional broad and weak peak at a  $q$ -value of about  $0.025 \text{ nm}^{-1}$ . This peak indicates that there are pronounced side-to-side positional correlations (251 nm) between the particles on a scale comparable to the particle diameter. For an  $N_D$  structure, the side-to-side positional correlations can be expected to be very much weaker than the face-to-face correlations due to the high aspect ratio of the particles. The pattern presented therefore better fits the nematic columnar ( $N_C$ ) structure, in which platelets are piled up in stacks and the stacks themselves form a nematic structure.<sup>36–38</sup>

Upon further decrease of the ionic strength to  $10^{-4}$  M, the sample at 300 g/L separates into two liquid crystal phases. The

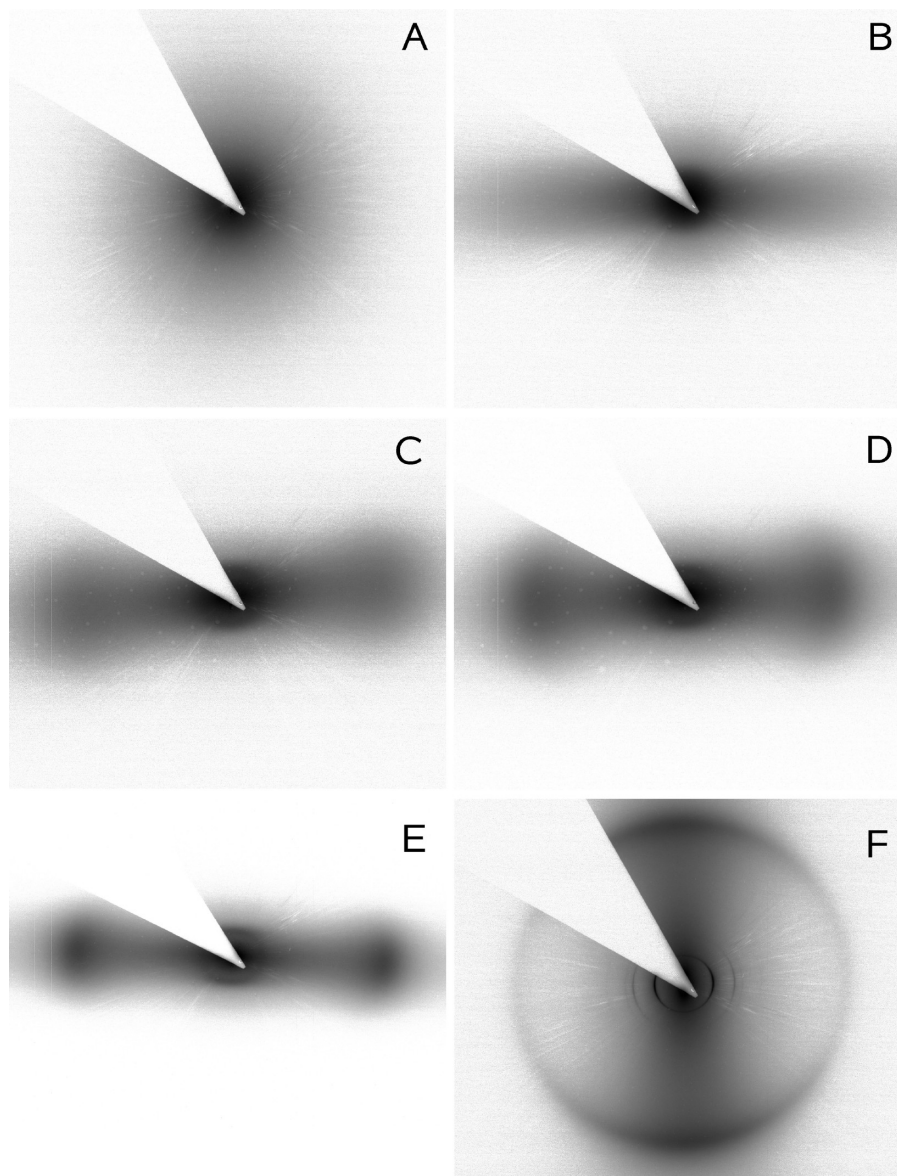


**Figure 5.** SAXS patterns of gibbsite dispersions at 300 g/L. Displayed are scattering patterns at a salt concentration of  $3 \times 10^{-2}$  M (panel A, isotropic upper phase; panel B, discotic nematic lower phase),  $10^{-2}$  M (panel C),  $10^{-3}$  M (panel D), and  $10^{-4}$  M (panel E, columnar nematic upper phase; panel F, hexagonal columnar lower phase).

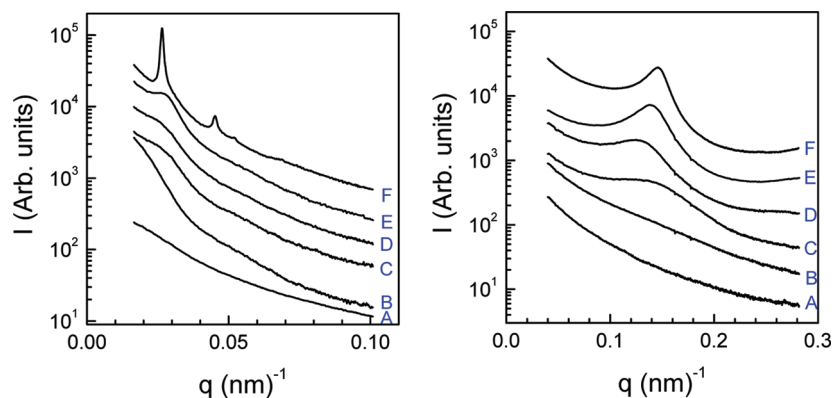


**Figure 6.** Profiles obtained by azimuthal integration of the 2D scattering patterns represented in Figure 5. In the left-hand panel, the sector of integration was along the orientations of the 100 peaks. For the right-hand panel, the sector of integration was selected along the orientations of the 001 peaks. The  $q$ -range of both graphs was selected to clearly visualize the peaks in the low  $q$ -range (left-hand panel) and high  $q$ -range (right-hand panel), respectively. The index letters in the graphs refer to the panels in Figure 5.

scattering pattern of the upper phase (Figure 5E) shows similarity to that of the sample at  $10^{-3}$  M, having anisotropy

and two broad peaks at  $q$ -values of about 0.026 and 0.143  $\text{nm}^{-1}$  (Figure 6, curve E) corresponding to 239 and 44 nm, respec-



tively. In contrast to the  $10^{-3}$  M sample, however, the peaks are more pronounced, especially for the side-to-side correlations.

In the bottom part of the sample at  $10^{-4}$  M (Figure 5F), we observe strong, sharp, and ring-like reflections at  $q = 0.026$  and  $0.045 \text{ nm}^{-1}$ . Closer inspection of the data reveals also weaker but sharp rings at  $q = 0.052$  and  $0.068 \text{ nm}^{-1}$  (Figure 6, curve F). These  $q$ -values are related to each other as  $1:\sqrt{3}:\sqrt{4}:\sqrt{7}$ , unambiguously confirming that they originate from the (100), (110), (200), and (210) Bragg reflections of the hexagonal columnar structure.<sup>36</sup> In addition, broader reflections at  $q = 0.143 \text{ nm}^{-1}$  and  $q = 0.287 \text{ nm}^{-1}$  correspond to the (001) and (002) intracolumnar scattering and arise from the (liquid-like) ordering of the platelets within the columns.

For the second series, we present diffractograms for 450 and 500 g/L at a fixed salt concentration of  $10^{-2}$  M in Figure 7, in addition to the scattering pattern of the sample at 300 g/L, presented in Figure 5c. Upon increase of concentration, the pattern yields a peak that refers to side-to-side positional correlations ( $q = 0.0292 \text{ nm}^{-1}$  for 450 g/L and  $q = 0.0296 \text{ nm}^{-1}$  for 500 g/L) and is most pronounced at largest particle concentration. Furthermore, pronounced broad peaks related to face-to-face correlation distances are visible ( $q = 0.180 \text{ nm}^{-1}$  for 450 g/L and  $q = 0.191 \text{ nm}^{-1}$  for 500 g/L). Although the SAXS patterns and positional ordering for these two samples are rather similar, rheologically, they are characterized as sol and gel, respectively.

In order to obtain a real space image of the gel structure at  $10^{-2}$  M salt, cryo-FIB-SEM experiments were performed on cryogenically immobilized dispersions. For this, a sample that was at even further distance from the sol–gel transition boundary at 600 g/L was used. A focused ion beam is used to create a cross section through the frozen droplet that allowed for inspection of the new interface by SEM. Figure 7C displays a SEM image of such a clean cross section created by focused ion beam milling. The platelets are light against a dark background, and their edges are seen; in other words, the platelets are aligned perpendicular to the plane of the image. The structure appears to be more ordered than a nematic phase; i.e., there is a distinct tendency of the platelets to form stacks. These stacks show capricious meandering that destroys any long-range periodical or orientational ordering within the area that is displayed in the SEM image. However, the spatial resolution of the images is too low to extract accurate positions and orientations of individual platelets.

Finally, the scattering patterns for the gel samples at high salt concentration ( $10^{-1}$  M) and a particle concentration of 100 and 200 g/L are displayed in Figure 8A and B. These show a qualitatively different structure in comparison with the scattering patterns of the other samples. In particular, a broad peak is found at very low  $q$ -values ( $q = 0.0098 \text{ nm}^{-1}$  for 100 g/L and  $q = 0.0102 \text{ nm}^{-1}$  for 200 g/L) that indicates the presence of a characteristic periodicity of 650 nm in the sample.

In order to obtain further information on the morphology of the attractive gel state, again cryo-FIB-SEM experiments were performed on a cryogenically immobilized dispersion. Again, electron micrographs could be taken of a cross section through the frozen droplet that was created by the focused ion beam (see Figure 8C). The micrographs display large structures composed of many gibbsite platelets that are touching each other and that are separated by large water-rich regions of typical size varying from 100 to 800 nm.

Quantitative results from the SAXS experiments within both the sol and repulsive gel region are presented as the variation of the typical interparticle distance with the overall gibbsite

concentration (Figure 9). The face-to-face distance is estimated as  $2\pi/q_{001}$ , where  $q_{001}$  is the position of the peak at larger  $q$ -values. The estimate of the side-to-side distance,  $4\pi/(\sqrt{3}q_{100})$ , was only possible for those structures possessing a sufficiently pronounced peak at a low  $q$ -value. The peak positions were determined whenever possible at the bottom of the capillaries, 1 month after their preparation.

In Figure 10, we combine the phase behavior as observed from birefringence, iridescence, and SAXS measurements to form a phase diagram.

#### 4. Discussion

From the rheological experiments, it follows that there is a sol region that is wedged between two gel regions: one at high salt concentration and one at low salt concentrations and high particle concentrations. This kind of sol–gel state diagram is typically found in rheological experiments on charged platelets.<sup>2,6,9,17</sup> The shape of the diagram suggests that in the high salt case attractions between the particles dominate, while in the low salt case the system is jammed in a repulsive gel.

For dispersions of gibbsite at low pH, as studied in this work, the faces and the edges of the particles have the same charge sign (positive).<sup>39</sup> In this case, the origin of the attraction is the van der Waals interaction which tends to dominate the electric double layer repulsion at a salt concentration of  $10^{-1}$  M or higher.<sup>41,42</sup> In the case of clays, the difference in face (negative) charge and edge (positive) charge (for a recent direct experimental confirmation of this phenomenon, see ref 40) leads to an additional source of attraction.<sup>23</sup> There, a minimum in the interaction curve already appears at  $10^{-2}$  M salt. This may explain why the turnover from repulsion dominated to attraction dominated interaction occurs at higher salt concentrations in the case of gibbsite than in the case of clays. Our results show that the formation of liquid crystal phases is essentially limited to the sol region of the rheological state diagram. This implies that, while thermodynamically liquid crystal formation may be favored in parts of the gel region, the system is kinetically arrested. This is in agreement with recent observations in liquid crystal formation on nontronite suspensions.<sup>6</sup>

A more detailed view on the structure of the dispersions was obtained by X-ray scattering and electron microscopy. One can see that the typical interparticle distances are mostly governed by the overall gibbsite concentration (Figure 9). This is understandable, since this concentration determines the amount of space available in the system. In principle, the ionic strength, which affects the details of the interparticle interaction, can influence the proportion of the free space between the faces of the particles compared to the free space between their sides. Our data, however, is not conclusive enough to resolve these effects of the salt concentration.

The SAXS measurements do indicate that the structure of the liquid crystal phases in the sol region strongly depends on the salt concentration: the lower the salt concentration, the more structure was found (Figure 5). At high salt concentrations, the nematic samples have anisotropic scattering patterns and decay monotonically from the center, as expected for a discotic nematic phase ( $N_D$ ). On lowering the salt concentration, first the face-to-face interparticle correlations appeared. On further lowering the salt concentration, apart from the face-to-face correlations, a gradual transformation of the structure from  $N_D$  to  $N_C$  can be seen. These two structures differ in the strength of the side-to-side positional correlation between the particles. In  $N_D$ , the positional correlations mainly exist between the faces of single platelets. The  $N_C$  structure consists of stacks of platelets, which

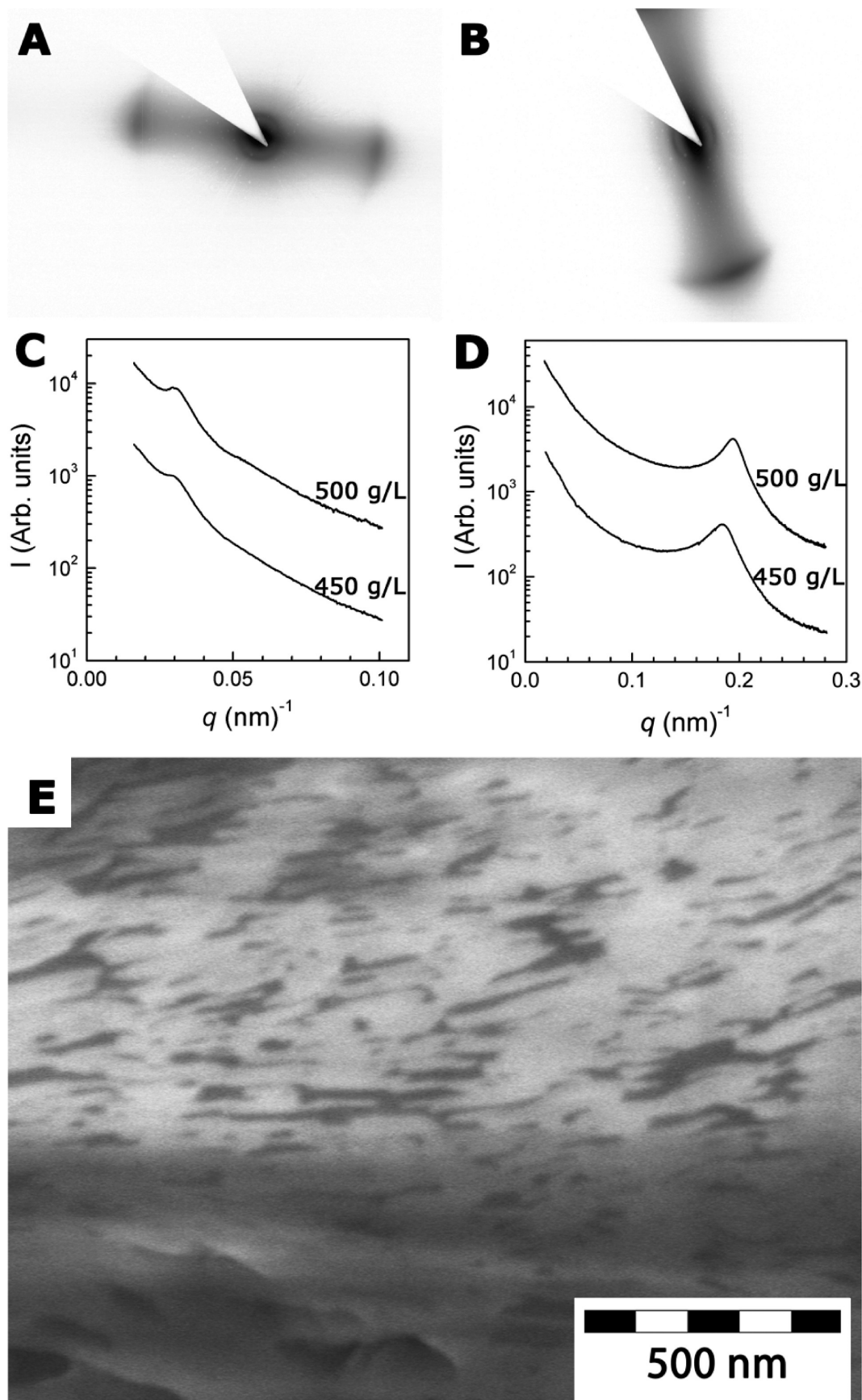


**Figure 7.** SAXS patterns at a salt concentration of  $10^{-2}$  M, 450 g/L (panel A) and 500 g/L (panel B). Profiles obtained by azimuthal integration of the scattering patterns in panels A and B are presented in panel C (with the sector of integration selected along the orientation of the 100 peaks) and in panel D (with the sector of integration selected along the orientation of the 001 peaks). In panel E, a scanning electron micrograph of a cryogenically immobilized dispersion with a salt concentration of  $10^{-2}$  M and a gibbsite concentration of 600 g/L is displayed.



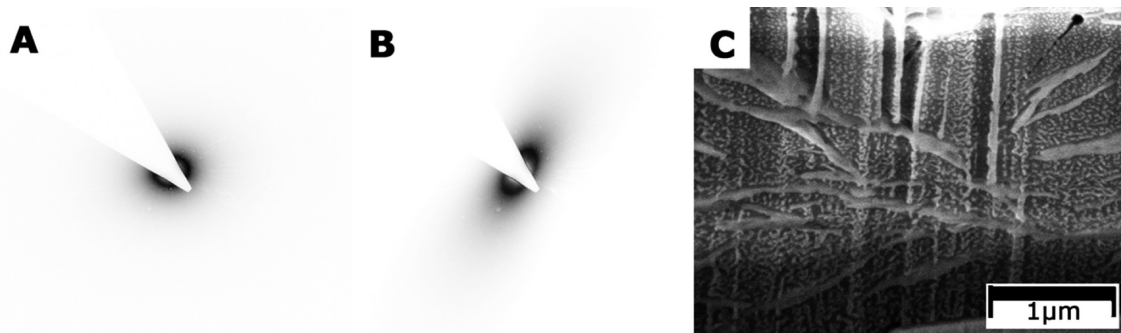


**Figure 8.** SAXS patterns at  $10^{-1}$  M, 100 g/L (panel a) and 200 g/L (panel b). In panel c, a scanning electron micrograph of a cryogenically immobilized dispersion with a salt concentration of  $10^{-1}$  M and a particle concentration of 200 g/L is displayed.

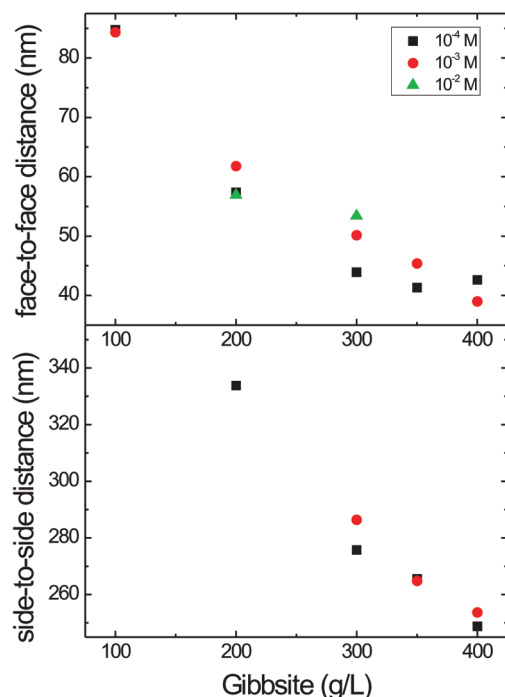


**Figure 9.** Variation of the typical face-to-face and side-to-side interparticle distances as a function of the overall gibbsite concentration. The typical distances are determined from the X-ray patterns as described in the text.

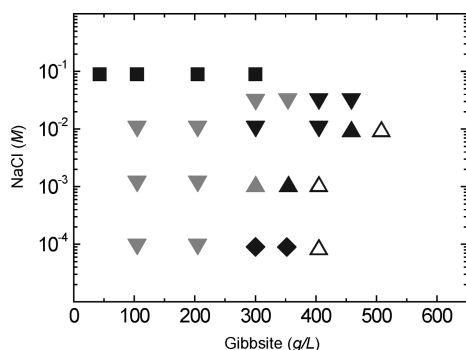


**Figure 10.** Phase diagram of aqueous gibbsite dispersions: (■) nonbirefringent gel states; (▼)  $N_D$  phases; (▲)  $N_C$  phases; (◆) C phases in coexistence with an  $N_C$  upper phase. Liquid crystal phases that are in coexistence with an isotropic phase are colored gray, while open symbols refer to repulsive gel states.

strengthen the side-to-side interparticle correlations, as is illustrated in Figure 11. Since we do not see any clear boundary between  $N_D$  and  $N_C$ , we choose the presence of both the face-to-face and the side-to-side correlation peaks in the scattering domain to assign the  $N_C$  structure. At the lowest ionic strength

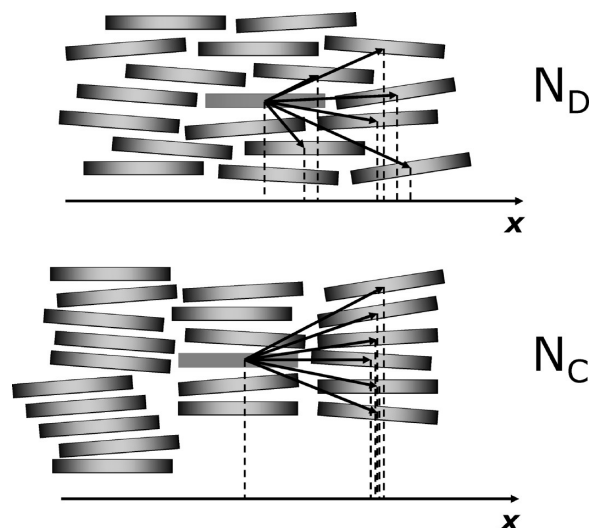


**Figure 11.** Schematic illustration of the  $N_D$ - and  $N_C$ -type structures which differ in the strength of the side-to-side positional correlations between the particles. While in the  $N_D$ -type structure there are few pairs of particles separated in the  $x$ -direction by the distance of approximately one particle diameter, for the  $N_C$ -type structure, this occurs for many more pairs of particles.

studied ( $10^{-4}$  M) and at sufficiently high particle concentration a hexagonal columnar phase (C) is found that is in coexistence with a nematic phase having an  $N_C$  structure. The  $N_C$  structure also occurs at a salt concentration of  $10^{-2}$  M, be it at higher particle concentration (450 g/L). Guided by the analogy with lowering the salt concentration, one would expect that upon further increase of the particle concentration a hexagonal columnar phase (C), possibly in coexistence with  $N_C$ , would appear. At 500 g/L, however, the structure remains  $N_C$ , but we have now entered the repulsive gel. This implies that the repulsive gel state has the signature of a metastable, kinetically arrested  $N_C$  state.

It is interesting to compare at what conditions the dynamical arrest occurs. From Figure 10, it appears that the location of the sol-attractive gel transition occurs at a salt concentration between  $3 \times 10^{-2}$  and  $10^{-1}$  M regardless of the overall colloidal gibbsite concentration. On the other hand, the location of the sol-repulsive gel transition which occurs at salt concentrations of  $10^{-2}$  M and below depends on the overall colloidal gibbsite concentration. The lower the salt concentration, the lower the gibbsite concentration at which the sol-repulsive gel transition occurs. In the vicinity of the sol-repulsive gel transition, both of the side-to-side correlation distances can be determined, since the structure is either hexagonal columnar or has a pronounced nematic columnar signature. In Table 1, the average distances for side-to-side correlations in the  $N_C$  phases are displayed for

**TABLE 1: Correlation Peaks and Distances Obtained by Small-Angle X-ray Scattering for Samples around the Sol–Gel Transition**

salt, M	gibbsite, g/L	state	$q_{100}$ , nm <sup>-1</sup>	side-to-side correlation distance, nm
10 <sup>-2</sup>	450	N <sub>C</sub>	0.0292	249
	500	repulsive gel	0.0296	245
10 <sup>-3</sup>	350	N <sub>C</sub>	0.0274	265
	400	repulsive gel	0.0286	254
10 <sup>-4</sup>	350	N <sub>C</sub>	0.0273	265
	400	repulsive gel	0.0294	247

the samples at the sol–gel transition boundary. For the correlation distances, local hexagonal ordering is assumed and the distance that follows from the peak for the side-to-side correlation is multiplied by a factor of  $2/(\sqrt{3})$ . These distances indicate that the structure is jammed when the columns of platelets are separated by approximately 250 nm, still considerably larger the platelet size (ECD, 205 nm). Therefore, we conclude that stack formation by the platelets is favored in dense dispersions and is even present in cases where the platelets are jammed due to a lack of space. At high salt concentrations, highly viscous gels are formed already at low gibbsite concentration. Even from their visual appearance (Figure 4), it is clear that these gels are different from the repulsive gels. The enhanced turbidity suggests that a larger-scale structuring must be involved. Moreover, the absence of birefringence reveals that no orientational ordering is present. Earlier, the formation of clusters larger than the particle size was reported for dispersions of laponite<sup>10</sup> and cloisite.<sup>5</sup> X-ray scattering experiments on gibbsite samples reveal a broad but pronounced peak corresponding to a correlation distance significantly larger than the particle size. This points toward a sponge-like structure of the attractive gel. Electron micrographs substantiate the existence of such clusters of gibbsite particles and water regions with a mesh size of hundreds of nanometers.

## 5. Conclusions

Positively charged aqueous colloidal gibbsite particles show sol–gel behavior similar to clays as they enter kinetically arrested states at both high and low salt concentrations. At intermediate salt concentrations, sols are formed up to particle concentrations as high as 500 g/L gibbsite. In this extended sol region, I–N and N–C liquid crystal phase equilibria are present, as can be distinguished by observation of birefringence and iridescence. SAXS experiments reveal that the nematic phases at high salt concentrations or low platelet concentrations are of the discotic nematic (N<sub>D</sub>) kind, while the nematic phases at low salt/high platelet concentrations are of the columnar nematic (N<sub>C</sub>) kind. SAXS and cryo-FIB-SEM measurements show that the repulsive gel also has the signature of a columnar nematic phase. At high salt concentrations (10<sup>-1</sup> M), a gel is formed, due to domination of attractive interactions. SAXS measurements and cryo-FIB-SEM indicated a sponge-like structure of the attractive gel that is in agreement with that in clay systems, be it at higher salt concentrations.

**Acknowledgment.** The authors thank Annemieke ten Brinke and Hans Meeldijk for their help in preparing the experiments. Esther van den Pol, Nicolas Vilayphiou, Dirk Detollenaere, Anatoly Snigirev, and Wim Bras are thanked for their assistance in the SAXS experiments. Chris Schneijdenberg and Mike Hayles are acknowledged for discussions. The Dutch Organization for Scientific Research (NWO) is thanked for support of M.C.D.M. and for beam time at the DUBBLE beamline, ESRF (Grenoble).

## References and Notes

- (1) Gabriel, J. C. P.; Sanchez, C.; Davidson, P. *J. Phys. Chem.* **1996**, *100*, 11139–11143.
- (2) Abend, S.; Lagaly, G. *Appl. Clay Sci.* **2000**, *16*, 201.
- (3) Michot, L.; Bihannic, I.; Porsch, K.; Maddi, S.; Baravian, C.; Mougél, J.; Levitz, P. *Langmuir* **2004**, *20*, 10829–10837.
- (4) Michot, L. J.; Bihannic, I.; Maddi, S.; Funari, S. S.; Baravian, C.; Levitz, P.; Davidson, P. *Proc. Natl. Acad. Sci. U.S.A.* **2006**, *103*, 16101–16104.
- (5) Shalkevich, A.; Stradner, A.; Bhat, S. K.; Muller, F.; Schurtenberger, P. *Langmuir* **2007**, *23*, 3570–3580.
- (6) Michot, L. J.; Baravian, C.; Bihannic, I.; Maddi, S.; Moyne, C.; Duval, J. e. F. L.; Levitz, P.; Davidson, P. *Langmuir* **2009**, *25*, 127–139.
- (7) Mouchid, A.; Delville, A.; Lambard, J.; Lécolier, E.; Levitz, P. *Langmuir* **1995**, *11*, 1942–1950.
- (8) Kroon, M.; Wegdam, G.; Sprik, R. *Phys. Rev. E* **1996**, *54*, 6541–6550.
- (9) Mouchid, A.; Lécolier, E.; Van Damme, H.; Levitz, P. *Langmuir* **1998**, *14*, 4718–4723.
- (10) Levitz, P.; Lécolier, E.; Mouchid, A.; Delville, A.; Lyonnard, S. *Europhys. Lett.* **2000**, *49*, 672–677.
- (11) Fossum, J. O.; Gudding, E.; Fonseca, D. d. M.; Meheust, Y.; DiMasi, E.; Gog, T.; Venkataraman, C. *Energy* **2005**, *30*, 873–883.
- (12) Ruzicka, B.; Zulian, L.; Ruocco, G. *Langmuir* **2006**, *22*, 1106–1111.
- (13) Brown, A.; Clarke, S.; Rennie, A. *Langmuir* **1998**, *14*, 3129–3132.
- (14) van der Beek, D.; Lekkerkerker, H. N. *Langmuir* **2004**, *20*, 8582–8586.
- (15) Mourad, M. C. D.; Wijnhoven, J. E.; G, J.; Van't Zand, D. D.; Van der Beek, D.; Lekkerkerker, H. N. W. *Philos. Trans. R. Soc., A* **2006**, *364*, 2807–2816.
- (16) Michot, L. J.; Ghanbaja, J.; Tirtaatmadja, V.; Scales, P. J. *Langmuir* **2001**, *17*, 2100–2105.
- (17) Zhang, J.; Luan, L. Y.; Zhu, W. X.; Liu, S. Y.; Sun, D. J. *Langmuir* **2007**, *23*, 5331–5337.
- (18) Darley, H.; Gray, G. R. *Composition and Properties of Drilling and Completion Fluids*, 5th ed.; Gulf Publishing Company: Houston, TX, 1988.
- (19) van Olphen, H. *Discuss. Faraday Soc.* **1951**, *11*, 82–84.
- (20) Mourad, M. C. D.; Byelov, D. V.; Petukhov, A. V.; Lekkerkerker, H. N. W. *J. Phys.: Condens. Matter* **2008**, *20*, 0953–8984, 494201.
- (21) Norrish, K. *Discuss. Faraday Soc.* **1954**, *18*, 120–134.
- (22) Schofield, R. K.; Samson, H. R. *Discuss. Faraday Soc.* **1954**, *18*, 135.
- (23) Jönsson, B.; Labbez, C.; Cabane, B. *Langmuir* **2008**, *24*, 11406–11413.
- (24) Onsager, L. *Ann. N.Y. Acad. Sci.* **1949**, *51*, 627–659.
- (25) Langmuir, I. *J. Chem. Phys.* **1938**, *6*, 873–896.
- (26) Thompson, D. W.; Butterworth, J. T. *J. Colloid Interface Sci.* **1992**, *151*, 236–243, 0021–9797.
- (27) Michot, L. J. Private communication, 2008.
- (28) Wijnhoven, J. E.; G, J.; van't Zand, D. D.; van der Beek, D.; Lekkerkerker, H. N. W. *Langmuir* **2005**, *21*, 10422–10427.
- (29) Hernandez, J. Ph.D. thesis, Université Pierre et Marie Curie, 1998.
- (30) Goodwin, J. W.; Hughes, R. W. *Rheology for Chemists. An Introduction*; Royal Society of Chemistry: Cambridge, U.K., 2000.
- (31) Petukhov, A. V.; Thijssen, J. H. J.; 't Hart, D. C.; Imhof, A.; van Blaaderen, A.; Dolbnya, I. P.; Snigirev, A.; Moussaid, A.; Snigireva, I. *J. Appl. Crystallogr.* **2006**, *39*, 137–144.
- (32) Snigirev, A.; Kohn, V.; Snigireva, I.; Lengeler, B. *Nature* **1996**, *384*, 49.
- (33) Hayles, M. F.; Stokes, D. J.; Phifer, D.; Findlay, K. C. *J. Microsc.* **2007**, *226*, 263–269.
- (34) Winter, H. H.; Morganelli, P.; Chambon, F. *Macromolecules* **1988**, *21*, 532–535.
- (35) Almdal, K.; Dyre, J.; Hvidt, S.; Kramer, O. *Polym. Gels Networks* **1993**, *1*, 5–17.
- (36) Laschat, S.; Baro, A.; Steinke, N.; Giesselmann, F.; Hägele, C.; Scalia, G.; Judele, R.; Kapatsina, E.; Sauer, S.; Schreivogel, A.; Tosoni, M. *Angew. Chem., Int. Ed.* **2007**, *46*, 4832–4887.
- (37) Praefcke, K.; Singer, D.; Kohne, B.; Ebert, M.; Liebmann, A.; Wendorff, J. H. *Liq. Cryst.* **1991**, *10*, 147–159.
- (38) Bengs, H.; Karthaus, O.; Ringsdorf, H.; Baehr, C.; Ebert, M.; Wendorff, J. H. *Liq. Cryst.* **1991**, *10*, 161–168.
- (39) Wierenga, A. M.; Lenstra, T. A. J.; Philipse, A. P. *Colloids Surf., A* **1998**, *134*, 359–371.
- (40) Zhao, H.; Bhattacharjee, S.; Chow, R.; Wallace, D.; Masliyah, J. H.; Xu, Z. *Langmuir* **2008**, *24*, 12899–12910.
- (41) Verwey, E. J. W.; Overbeek, J. Th. G. *Theory of the Stability of Lyophobic Colloids*; Elsevier: Amsterdam, The Netherlands, 1948.
- (42) Israelachvili, J. N. *Intermolecular and Surface Forces*; Academic Press: New York, 1991.